Perforated Lamellae Morphology in Novel P2VP(PDMS-b-PI-b-PS)₂ 3-Miktoarm Star Quarterpolymer

Jacob Judas Kain Kirkensgaard,*,† Panagiota Fragouli,‡ Nikos Hadjichristidis,‡ and Kell Mortensen†

†*Department of Basic Sciences and Environment, Faculty of Life Sciences, University of Copenhagen, Copenhagen, Denmark, and* ‡*Department of Chemistry, University of Athens, Panepistimiopolis-Zografou, Athens, Greece*

ABSTRACT: The melt morphology of a novel P2VP(PDMS-b-PI-b-PS)₂ 3-miktoarm star quarterpolymer is investigated. The melt morphology is determined using rheology and small-angle neutron and X-ray scattering data in conjunction with dissipative particle dynamics simulations of a model molecule matching the volume fractions of the experimental system. The simulations are used to interpret the scattering data and identify the melt morphology as a new perforated lamellae structure. In this structure the P2VP forms hexagonally perforated lamellae containing close-packed protrusions of PS connecting adjacent lamellae layers of PS. The PI part forms a lining between the P2VP and PS domains constrained by the molecular architecture.

Introduction

The study of molecular self-assembly remains a topic of great attention in material science as well as in biology and biotechnology. Special interests concern self-assembly properties of the variety of novel complex block copolymer architectures that modern chemistry allows, ABC 3-miktoarm star terpolymers being one example. Here three different polymer chains are attached to a common junction,[1,2] and the constraints imposed by the molecular star architecture have already been shown to induce a range of interesting morphologies and properties, among these various cylindrical structures whose cross-sectional organization follow Archimedean tiling patterns[3−13] or even show quasi-crystalline features.[14,15] Further, it has recently been speculated that these new block copolymer architectures will lead to other novel ordered structures with attractive characteristics, for example, being cholesteric,[16] forming complex network phases,[17] or resulting in various hierarchically structured morphologies.[18]

In this study we investigate a new miktoarm block copolymer, the 3-armed star quarterpolymer P2VP(PDMS-b-PI-b-PS)₂ illustrated schematically in Figure 1. Here the complexity of the 3-miktoarm star topology is raised even further as two arms consist of equivalent (PDMS-b-PI-b-PS)-triblocks and the third arm of a single P2VP polymer species. We investigate the melt morphology of this miktoarm star using combined dissipative particle dynamics simulations (DPD) and experimental structural analysis using simultaneous small-angle neutron scattering and rheology (rheo-SANS) as well as small-angle X-ray scattering (SAXS).

DPD is a mesoscopic simulation technique where a "particle" represents a small volume of fluid which interacts with other particles through a soft potential. In its most common implementation[19] the DPD method has become a standard tool in soft matter research and has been applied successfully to a number of polymeric systems with varying structural complexity.[20−25]

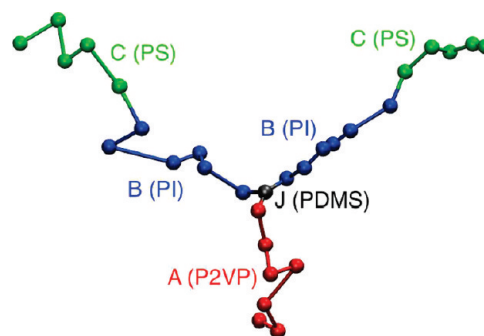*Corresponding author. E-mail: kirkensgaard@life.ku.dk.

Figure 1. Rendering of the model 3-miktoarm star molecule as represented in the DPD simulations. The volume fractions of the different blocks are reflected in the relative arm lengths set to 1:5:6:7 for PDMS (gray junction J), PS (green C), PI (blue B), and P2VP (red A), respectively (see Table 2).

The experimental determination of the melt morphology is done using small-angle neutron scattering (SANS) and *in situ* rheology with a modified rheometer allowing simultaneous determination of structural and dynamic mechanical properties as well as the response to large-amplitude oscillatory shear (LAOS). As has been frequently shown, LAOS has the ability to dramatically change the texture of ordered soft matter materials and in some cases produce close to single-domain crystallographic structures (see for example refs 26 and 27). The shear-aligned samples are subsequently also investigated with SAXS.

This paper is organized as follows: First, the polymer synthesis and characteristics are described. Second, we briefly outline the model used in the simulations and describe the details of the experimental procedures. We then present the structures predicted by the DPD simulations followed by rheological and structural data where the latter is shown to be consistent with only one of two possible structures predicted by the simulations.
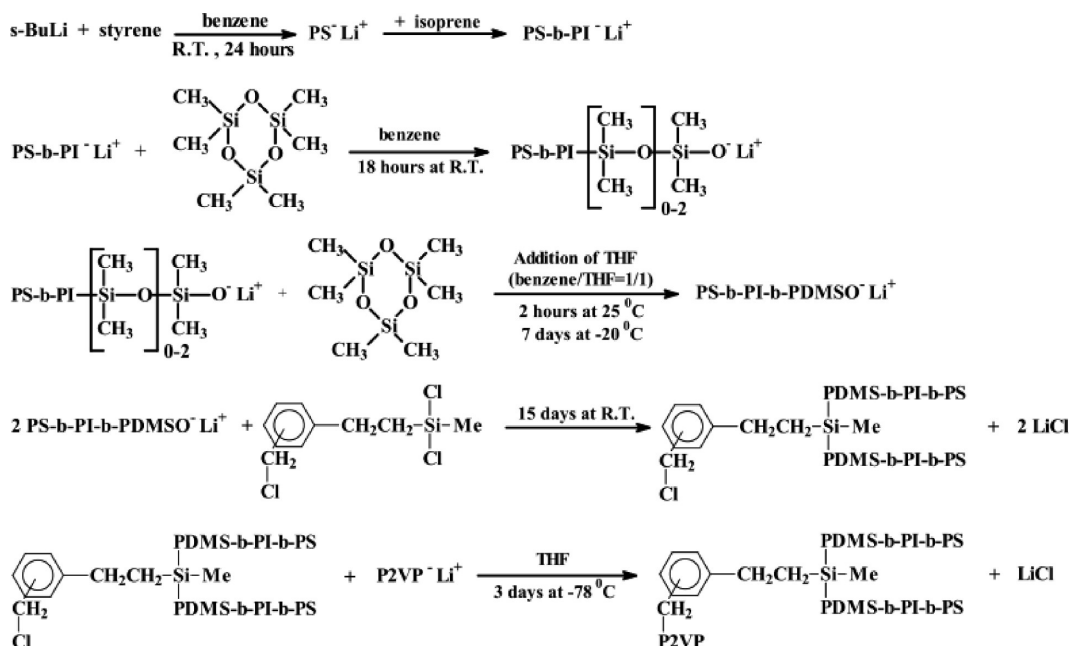
Figure 2. Synthesis of 3-miktoarm star quarterpolymer P2VP(PDMS-*b*-PI-*b*-PS)₂.
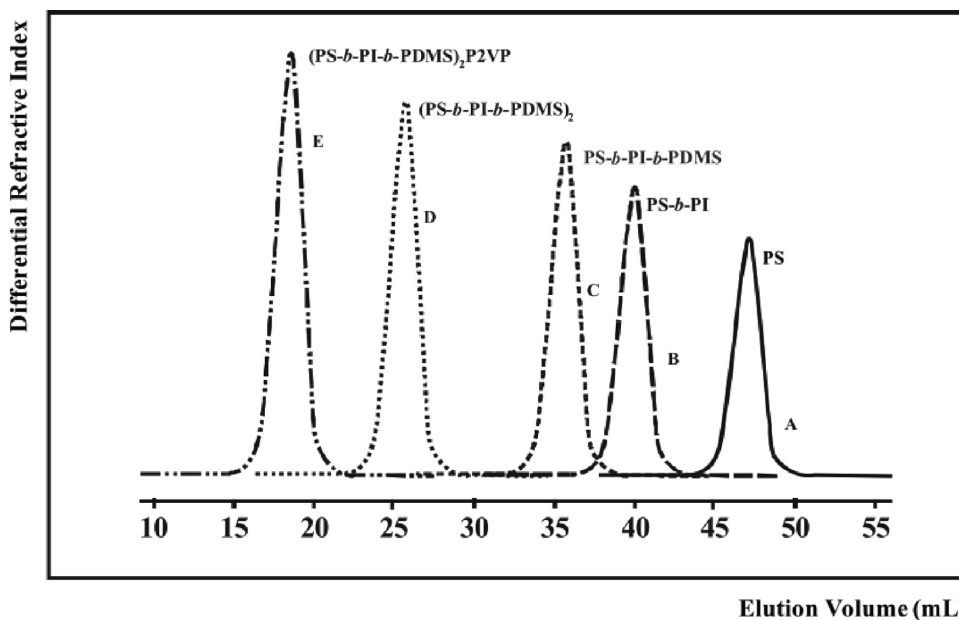

Figure 3. Monitoring the steps of the synthesis of the 3-miktoarm star quarterpolymer by size exclusion chromatography (SEC): (A) PS block, (B) PI-*b*-PS diblock, (C) PDMS-*b*-PI-*b*-PS precursor, (D) (PDMS-*b*-PI-*b*-PS)₂ precursor, and (E) final P2VP(PDMS-*b*-PI-*b*-PS)₂ star quarterpolymer.

Polymer Synthesis and Molecular Characterization

The synthesis of the 3-miktoarm star quarterpolymer P2VP-(PDMS-*b*-PI-*b*-PS)₂ was based, on one hand, on recent advances in the controlled high-vacuum anionic polymerization of hexamethylcyclotrisiloxane (D₃)[28] and, on the other hand, on the selective linking of PDMSOLi or PDMSOLi-terminated chains with the chlorosilane groups of the heterofunctional linking agent chloromethylphenylethenyldichloromethylsilane (CMPMDS).[29] The synthetic approach involves the replacement of the two chlorines (SiMeCl₂) of CMPMDS by PDMS-*b*-PI-*b*-PS triblock terpolymer chains and of the remaining chlorine (CH₂Cl) by P2VP.[30]

The basic reactions for the synthesis are given in the scheme in Figure 2, and the molecular characteristics of the precursors and final miktoarm star based on the SEC runs presented in Figure 3

Table 1. Molecular Characteristics of Precursors and Final 3-Miktoarm Star Quarterpolymer

polymer	M_n [kg/mol]	M_w/M_n
PS	13.6[a]	1.02[a]
PI-*b*-PS	26.8[b]	1.03[a]
PDMS-*b*-PI-*b*-PS	29.5[b]	1.04[a]
(PDMS-*b*-PI-*b*-PS)₂	57.8[b]	1.04[a]
P2VP(PDMS-*b*-PI-*b*-PS)₂	77.8[b]	1.04[a]

[a] SEC in THF at 40 °C calibrated with PS standards. [b] Membrane osmometry in toluene at 35 °C.

are summarized in Table 1. All polymerizations were carried out in evacuated, *n*-BuLi-washed, and solvent-rinsed glass reactors, equipped with break-seals for the addition of reagents and constrictions, for the removal of intermediate products. Full details

Table 2. Molar Mass M_n [kg/mol] of Each Polymer Component, Densities ρ [g/cm^3], Volume Fractions in the Experiments (ϕ), Ratios Relative to Volume Fraction of PDMS, and Volume Fractions in the Simulations (ϕ_{DPD})

polymer	M_n	ρ	ϕ	ϕ/ϕ_D	ϕ_{DPD}
PDMS	2.7	0.965	0.05	1.0	1
PS	13.6	0.969	0.26	5.0	5
PI	13.2	0.830	0.3	5.7	6
P2VP	20	0.97	0.39	7.4	7

regarding apparatuses and techniques used have been reported elsewhere.[31]

Simulation Model

On the basis of the molecular weights of the P2VP(PDMS-*b*-PI-*b*-PS)$_2$ 3-miktoarm quarterpolymer shown in Table 2, we set up the coarse-grained model illustrated in Figure 1 where the number of beads of each color directly reflects the volume fractions of the different blocks relative to the minority component PDMS. Although a detailed mapping of the interactions between different polymer species in principle is possible via a link with Flory−Huggins theory,[32] we will employ a purely qualitative approach and present only two scenarios that give results of relevance to the scattering data presented below. One scenario is assuming symmetric interactions between all unlike polymer components, and the other is assuming that the interaction parameter between the red A and the blue B component is higher. This reflects the fact that the interaction parameter between P2VP and PI is usually found to be higher than the other cross interaction terms which are roughly equal.[5,24,33,34] In terms of the DPD interaction parameter a_{ij}, we set this to 36 between all different species i and j in the first scenario and then raise a_{AB} to 45 in the second scenario. Other numbers have also been used yielding the same structures. For complete details of the simulations presented here we refer to ref 35 where a comprehensive simulation study of this star architecture is presented. Simulations were run using the ESPResSo package[36] within the framework developed earlier to simulate the equilibrium structure of branched molecules in general.[16]

Rheo-SANS and SAXS

SANS experiments and rheology measurements were performed using a modified Rheometrics RSA II rheometer at the SANS-II instrument at the Swiss Spallation Neutron Source (SINQ) located at the Paul Scherrer Institute, Switzerland. The setup allows simultaneous determination of dynamic mechanical and structural properties as well as structural response to LAOS. The employed neutron wavelength was 6 Å with a 9% wavelength spread. The sample−detector distance and the collimation length were both 4 m. The polymer samples were mounted in a sandwich shear cell of 0.1 mm thickness as illustrated in Figure 4 and subjected to various rheological measurements as well as LAOS.

Referring to Figure 4, we acquire two-dimensional SANS patterns in the (q_e, q_v) scattering-plane, where the indexes e refer to the neutral vorticity direction and v to the shear-velocity direction. After shear alignment the sample was quenched with liquid nitrogen to ambient temperature. The shear cell was mechanically fixed and remounted to perform crystallographic measurements using a custom-designed goniometer. The shear alignment and subsequent crystallographic measurements were performed with slight modifications on three independent sample outtakes, and the results obtained were identical within experimental error. The quenched and shear-aligned samples were saved and used for SAXS measurements done at room temperature. The SAXS measurements were done at the new SAXSLab
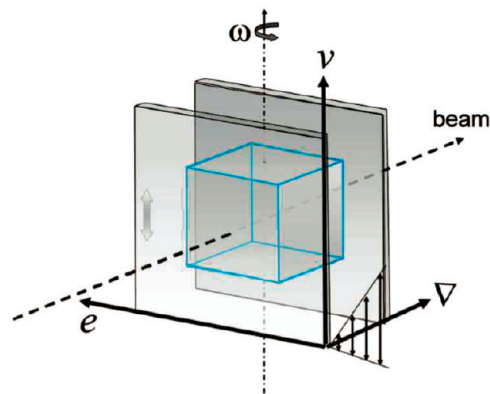

Figure 4. Schematics of the experimental *in situ* rheo-SANS setup defining the principal axes: flow direction v, gradient direction ∇, and neutral direction e. Chrystallographic measurements are done rotating angles ω around the flow axis v.
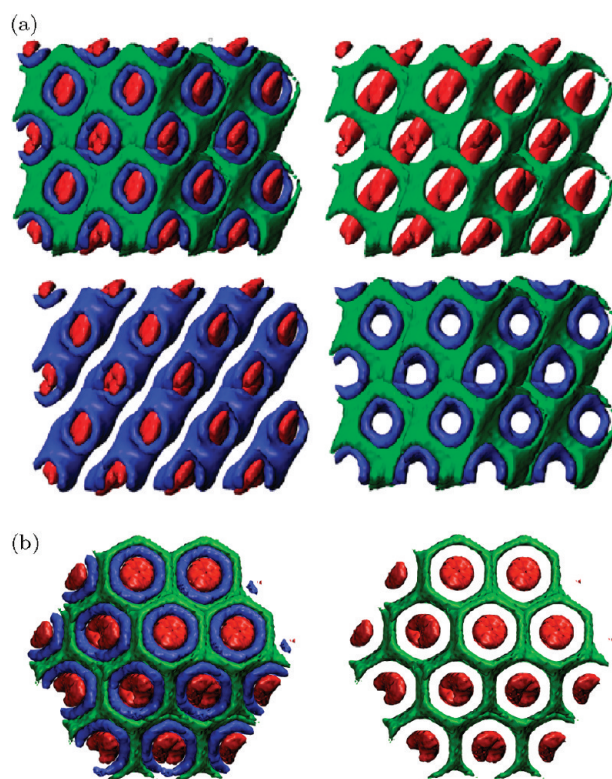

Figure 5. DPD simulation result split into pairs of colors. (a) For symmetric interactions, the red A (P2VP) component forms perforated lamellae (seen here edge on) with protrusions of green C (PS) connecting adjacent layers of green C (PS). The blue B (PI) component forms a lining between the red A (P2VP) and green C (PS) constrained by the molecular topology. (b) When raising the interaction parameter between the red A and blue B component, the simulation predicts a cylindrical core−shell structure. Images are based on 8 ($2 \times 2 \times 2$) simulation boxes.

facility at Copenhagen University employing a 1.54 Å wavelength.

Results and Discussion

Simulations. The self-assembled structures from the 3-miktoarm star predicted by the DPD simulations are shown in Figure 5 where the colors correspond to the ones used in Figure 1. In this particular system the volume fraction of the PDMS is small compared to the other components so for
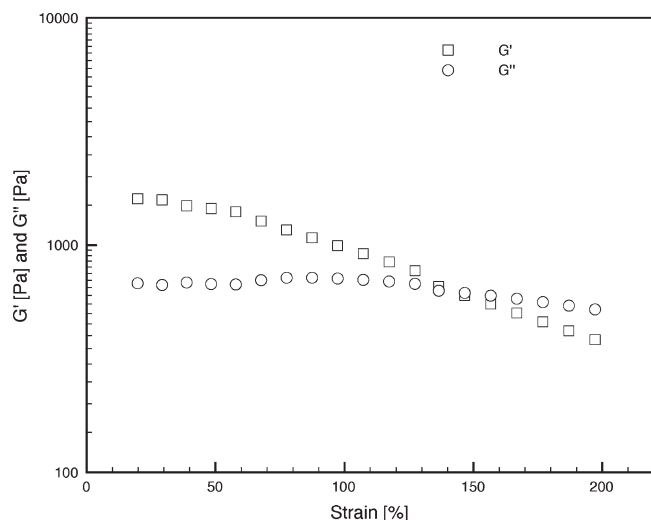
Figure 6. Rheological data showing the strain dependence of the elastic modulus G' and loss modulus G'' at $T = 200$ °C and shear frequency $\omega = 1$ Hz.

Figure 7. Temperature dependence of the elastic modulus G' and loss modulus G'' from measurements with frequency $\omega = 1$ Hz and shear amplitude $\gamma = 2\%$.

visual clarity we omit this component in the structural images shown in Figure 5. The PDMS part simply forms a thin lining between the red and blue domains. Assuming symmetric interactions, the resulting morphology is shown in Figure 5a. This structure has perforated lamellae of the red A (P2VP) component with the perforations arranged hexagonally in each plane and the overall packing of the perforations being fcc. Through the perforations protrusions of green C (PS) connects adjacent lamellae of green C (PS). The blue B (PI) component forms a lining between red A (P2VP) and green C (PS) constrained by the molecular architecture. As is shown in ref 35, this structure is robust in terms of modest variations of both (symmetric) interactions and relative arm lengths in this star architecture. Thus, there is good reason to assume this structure to be a candidate equilibrium morphology of the system studied experimentally, even though the detailed interaction parameters are not exact. On the other hand, as mentioned above, the interaction parameter between P2VP and PI is usually considered to be higher than that between PI−PS and PS−P2VP. Increasing the simulation interaction parameter between red A and blue B, the resulting morphology is a core−shell cylindrical structure shown in Figure 5b. With the employed volume fractions no other structures are predicted from the simulations. Further, given the scattering data shown below, these two structures are clearly feasible candidates for the melt morphology of the experimental system so we will focus on these.

Rheology and Scattering from Nonaligned Samples. Figures 6 and 7 shows rheological data from the P2VP(PDMS-*b*-PI-*b*-PS)$_2$ 3-miktoarm star quarterpolymer, as obtained at $T = 200$ °C, well above any of the components glass-transition temperature. The strain sweep shows a crossover from dominating elastic character to dominating dissipative character for strain amplitudes of the order of 100−150%, which is a typical value also observed for simple linear block copolymers. The temperature dependent moduli in Figure 7 shows a significant softening between 100 and 200 °C and a leveling off in the elastic value between 200 and 300 °C (the jump around 200 °C is due to the data being obtained on two different sample outtakes). There is no signature of any marked phase transition, which is also verified by the structural characteristics presented in Figure 8.
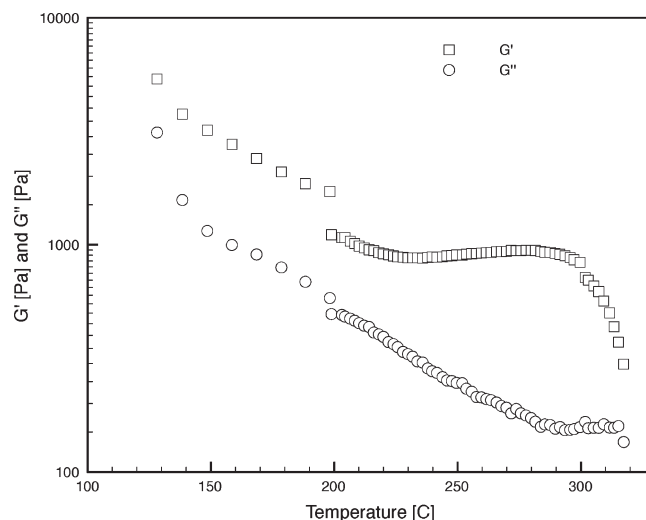
The azimuthally averaged scattering function is shown in Figure 8a. The intensity is dominated by three peaks at q^*, $2q^*$, and $3q^*$ with $q^* \sim 0.023$ Å^{-1} indicating dominating lamellar structure with a characteristic repeat distance around 275 Å. With good will there could be indications of hexagonal $(3)^{1/2}$ and $(7)^{1/2}$ peaks, but the limited resolution does not allow a definite answer to this. The scattering peak intensity (Figure 8b) decreases gradually to ~65% by raising the temperature from $T = 100$ °C to $T = 318$ °C, while the peak position, q, and peak width remain basically unchanged. At $T \approx 300$ °C, the shear modulus seems to vanish, which may indicate the proximity of an order-to-disorder phase transition (see Figure 7), although the scattering function does not show indications of any transition up to $T = 318$ °C. However, at $T \approx 300$ °C the sample is chemically unstable, and any conclusion on phase changes is therefore doubtful at these temperatures.

Scattering from Shear-Aligned Samples. The structural determination relies on rotation studies of the shear-aligned samples, and both the neutron and X-ray scattering from one of these are shown in Figure 10. Chronologically the SAXS measurements were done almost a year after the SANS measurements in order to gain additional information from the altered contrast conditions. The SAXS data are seen to be in accordance with the SANS data and so illustrate that the morphology of the quenched samples are stable at room temperature for many months. Since the initial alignment was done using the *in situ* rheo-SANS setup, we will start with looking at the SANS data and also discuss how these rule out the cylindrical structure predicted from the DPD simulations. Following this we look at the full set of data and describe crystallographic model calculations based on the perforated lamellae structure predicted from the DPD simulations and show that these agree with both the SANS and SAXS data, thus lending strong support for this structure as the morphology of the P2VP(PDMS-*b*-PI-*b*-PS)$_2$ 3-miktoarm quarterpolymer.

Starting with the cylindrical structure, let us assume this is the correct structure. It is clear that the dominating feature of all the SANS data is the first-order peak lying along the *e*-direction. This would then indicate that the cylinders are preferentially aligned along the flow axis. This leaves two possibilities for the behavior of the scattering patterns when rotating the sample around the flow axis. First, the cylinders
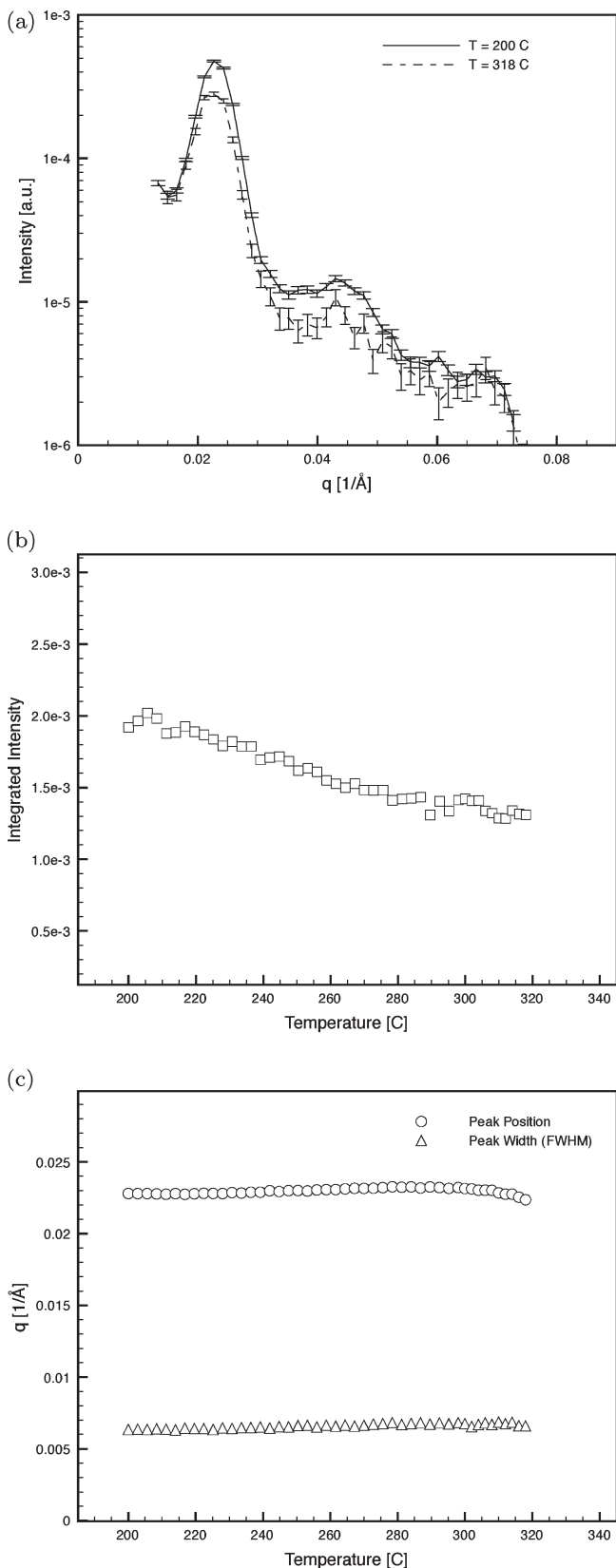
(a)

(b)

(c)

Figure 8. Temperature dependence of structural parameters. (a) Azimuthally averaged scattering function before shear alignment. (b) Integrated intensity for $q \in [0.015, 0.03]$ Å^{-1}. (c) Peak position and peak width (full width half-maximum).

could all be positioned randomly in the $e-\nabla$ plane, but then all rotations should give equivalent scattering patterns, which is clearly not the case. The other option is that the 90° data
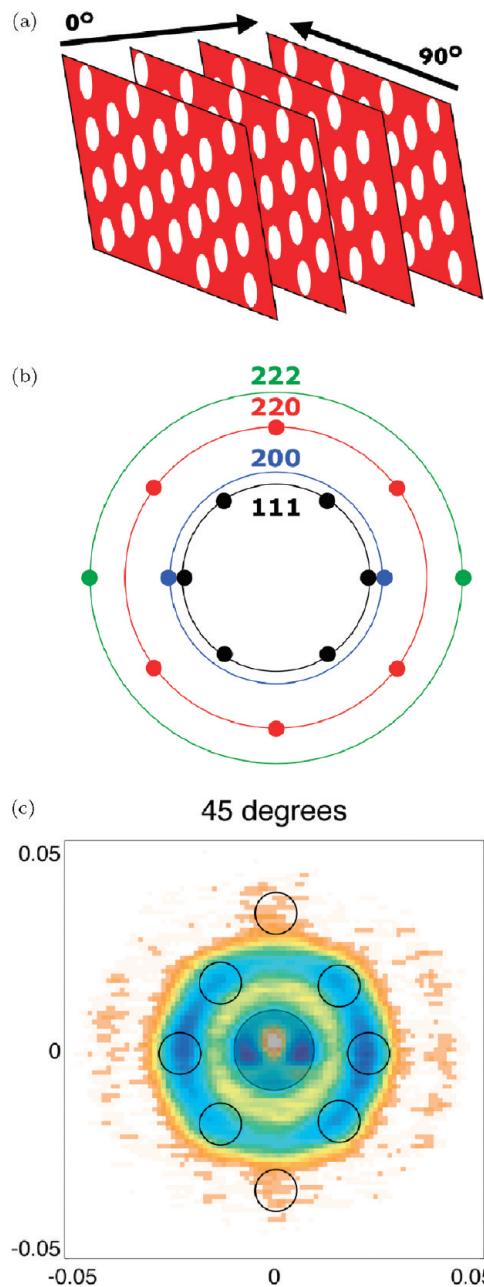
(a)

(b)

(c)

Figure 9. (a) Illustration of the fcc packing of the perforated lamellae of the DPD structure and how this is related to the scattering beam directions. (b) Illustration of all relevant crystallographic reflections from the rotation of a fcc crystal corresponding to (a). (c) Indications of (111) and (220) peaks in the 45° SANS data discussed in more detail below (axis units are Å^{-1}).

result from shooting parallel to the cylinder planes, but then the scattering pattern should be the same when rotating 60°; i.e., the 30° and 90° data should be equivalent, which again is not the case. Further, if the cylinders are preferentially aligned along ν, then we would expect a different scattering pattern to emerge if shooting neutrons along the flow axis ν but this is not the case—these data (not shown) are indistinguishable from the 90° data shown in Figure 10. Thus, it seems clear to conclude that the data are not consistent with the cylindrical structure or in fact with any type of modulated cylindrical structure[37,38] where the same arguments would apply. Also, the same line of reasoning could be practiced with the SAXS data.
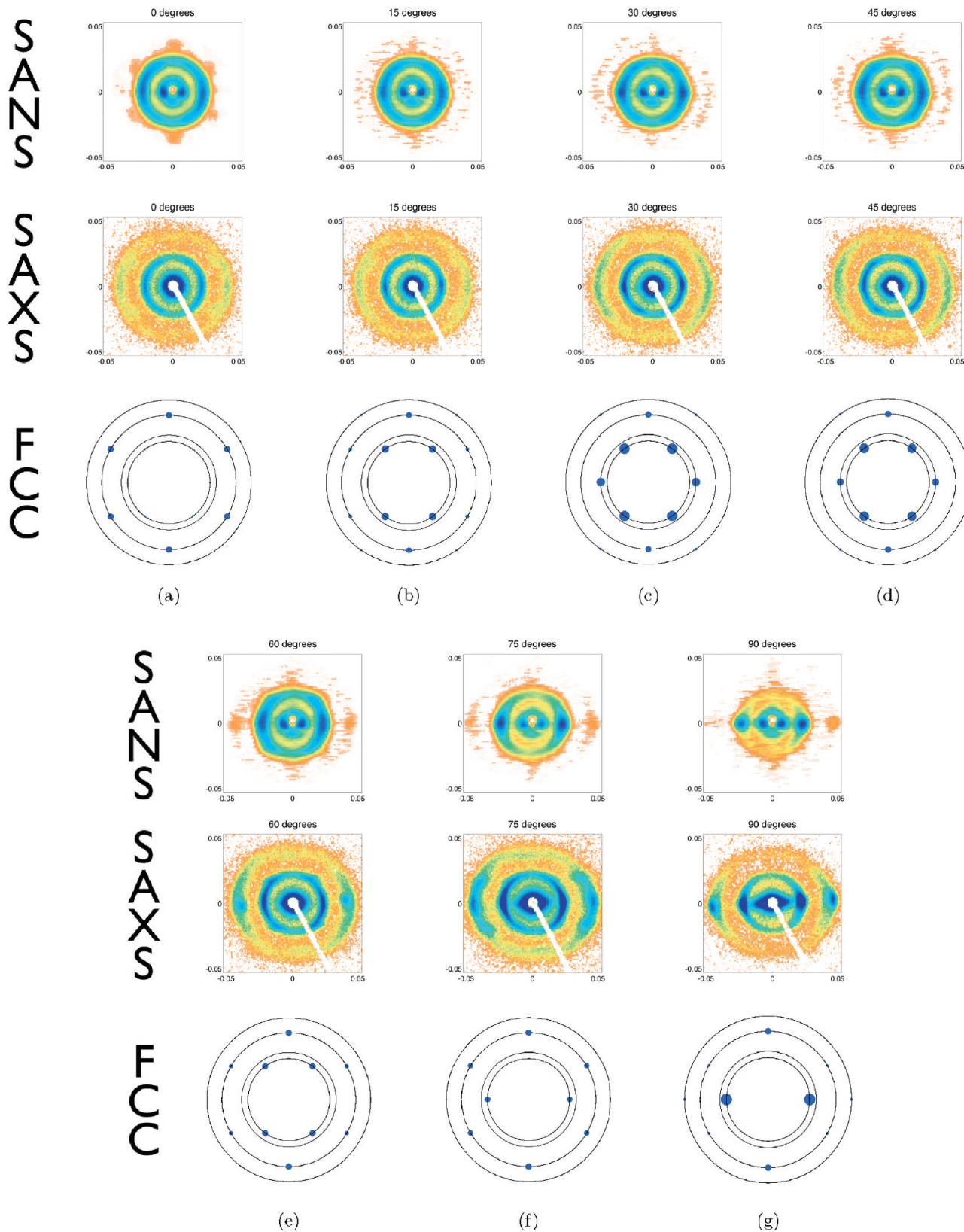
Figure 10. SANS and SAXS data from shear-aligned P2VP(PDMS-*b*-PI-*b*-PS)$_2$ 3-miktoarm quarterpolymers at different rotations and crystallographic model calculations from a fcc structure. Rotation 0° corresponds to the (*v,e*)-scattering plane, while rotation 90° corresponds to the (*v*, ∇)-scattering plane. Intensity is shown on a logarithmic scale with values ranging from 0 to 5, and axis units are Å^{-1} (note that the inner peaks in the SANS data are the forward scattering around the beamstop).

In contrast, the data are quite similar to measurements on diblock copolymers previously published in ref 27 where the structure is assigned as a perforated lamellar structure. There

the experimental observations were compared with the calculated scattering patterns from one or more crystalline domains of fcc symmetry. Here we perform corresponding

calculations adopting the symmetry of the perforated lamellae structure predicted from the DPD simulations. In Figure 8a we illustrate the relation between the DPD structure, the scattering directions and the crystallographic calculations. To accommodate the 90° data, the perforated lamellae have to be aligned parallel with the shearing planes and thus perpendicular to the beam direction at 0° rotation. As mentioned, the DPD simulations predicts that the perforations are packed as fcc, so in the model calculations we assume fcc symmetry with the [111] direction coinciding with the 0° beam direction, i.e., along the ∇ axis. We then rotate the structure 90° around the [$\bar{1}$10] directions in steps of 15° matching the experimental procedure. The calculations are done assuming a crystal mosaicity of 10°, and the size of the calculated reflections in Figure 10 scales with the distance between the reflection and the ideal Bragg condition. In Figure 8b we illustrate the relevant reflection families found in the calculations, and below that in Figure 8c a marked version of the 45° SANS data is shown, indicating these reflections as they appear in the data. Also, in Figure 8c the central part of the data has been masked out, illustrating that the inner peaks here are to be ignored since this stems from forward scattering around the beamstop.

Referring now to Figure 10, the figure is structured so that each of the panels a−g contain three images with the SANS pattern, SAXS pattern, and crystallographic model calculation arranged from top to bottom, respectively, and corresponding to the rotation in question. Each line is labeled clearly in the figure. The different patterns correspond to various rotations around the shear-velocity direction. The pattern indexed 0° corresponds to the (e, v)-plane while the pattern indexed 90° corresponds to the (∇, v)-plane (see Figure 4). Because of the highly asymmetric planar sample geometry during the SANS experiments, with the sample situated inside the shear fixture, we were not able to resolve the relative intensities, only the three-dimensional position in q-space. Different routes were tried to obtain optimal texture for unique determination of the ordered phase. These include studies at different temperatures between 120 and 318 °C as well as varying shear amplitudes and frequencies. All attempts resulted in the same structure and only minor variation in texture. In no case did we get perfect single-domain or corresponding simple texture, but the two-dimensional scattering pattern showed marked texture overlaid with a more or less significant contribution from non-oriented domains. The pattern obtained in the perpendicular (q_v,q_∇)-scattering plane (see 90° SANS data in Figure 10g) gives the best measure of the degree of aligned texture (there is a small asymmetry in the data from the edge-on 90° data due to scattering from the shear cell edges). These patterns shows very well resolved reflections, including higher order scattering peaks, which strongly indicate a dominating lamellar structure. Thus, this configuration gives a very good indication of the degree of shear-induced alignment as there is a clear underlying isotropic Debye−Scherrer scattering ring, but this is still an order of magnitude below the intensity of the 3D-resolved Bragg peak. The apparent dominance of the first-order lamellar peak is not only a matter of limited aligned texture. It is highly dominated by the effect of the form factor which reduces the intensity dramatically at high q-values.

Starting at 0° or in the (q_v, q_e)-scattering plane, which is the natural plane of *in situ* investigations with our instrument, the powder contribution dominates, but a distinct hexagonal pattern appears in the SANS data at large q-values corresponding to the (220) type of fcc reflections. In this configuration these (220) reflections are the only ones to be

expected from the shear-aligned domain as shown in the theoretical calculations. This is in fact strong evidence of the fcc symmetry from the ABCABC-type stacking of the perforations since for example a hexagonally close-packed ABABAB stacking would predict the (111) peaks to be dominating (tested, not shown). These reflections are also visible in the SAXS data although weaker since here the powder contribution is even stronger, clearly displaying both first- and second-order lamellar peaks.

When we start to rotate the sample several things are worth noting. For various rotations the calculations predict 4-fold (111) reflections to appear at ∼55° over the horizontal axis. These can both be seen in the SANS and SAXS data, weakly in the SANS data at rotation angles of 15°, 30°, 45°, and 60° and more clearly in the SAXS data. This is in total agreement with the model calculations, also the increasing intensity of the reflections in the 30° and 45° data compared to the 15° and to some extent 60° data. These reflections disappear at 75° and 90° as also predicted by the fcc model calculations. Further, for all rotations the (220) peaks along the v axis are predicted to be seen which we also have indications of in all SANS rotations. These are not seen in the SAXS data though which we ascribe to either or both the different contrast conditions and increased dominance of the powder part of the scattering. On the contrary, the SAXS data remarkably capture the off-meridional (220) reflections predicted for particularly the 75° rotation. Also, as we approach the 90° rotation, the horizontal (111) reflections increasingly dominate until finally these are the only peaks to be expected also in agreement with both SANS and SAXS data. In the model calculations the (222) reflections are probably represented too weakly which is in part due to the chosen peak size scaling. Overall, the observed scattering patterns are in very good agreement with the calculated pattern from a perforated lamellar phase where the perforations are ordered in a fcc structure, as also previously observed in linear diblock copolymers,[27,39−41] and thereby in agreement with the perforated lamellae structure predicted on the basis of the DPD simulations discussed above.

Conclusions

In conclusion, we have shown that by combining DPD simulations, rheo-SANS, and SAXS, the determination of the melt morphology of a newly synthesized 3-miktoarm star quarterpolymer, the P2VP(PDMS-*b*-PI-*b*-PS)$_2$, has been possible. The resulting morphology is shown to be a novel perforated lamellae structure with hexagonally perforated lamellae of P2VP containing close-packed protrusions of PS connecting adjacent lamellae layers of PS. The PI part forms a lining between the P2VP and PS domains constrained by the molecular architecture. We believe this is the first experimental report of this morphology in the literature.

Further, it is interesting to speculate if the increased molecular complexity represented by this new polymer system has helped increase the stability of the perforated lamellae phase. The question of the stability of perforated lamellae phases has been the subject of some interest in diblock copolymer systems.[39−55] Also, due to its topology, these structures have interesting perspectives as functional soft materials since one might selectively remove one component and thus for example generate continuous structures with well-defined nanopores.[27]

Finally, we have shown that results from DPD simulations on complex architectured copolymers are in good agreement with experimental results and can thereby be used effectively as a guidance for design of novel structured polymer materials. This concerns for example exciting new morphologies predicted in

ref 35 such as a potentially chiral gyroidal single network structure and a combined network and sphere packing structure.

References and Notes

(1) Hadjichristidis, N.; Iatrou, H.; Pitsikalis, M.; Pispas, S.; Avgeropoulos, A. *Prog. Polym. Sci.* **2005**, *30*, 725–782.
(2) Hadjichristidis, N.; Pispas, S.; Floudas, G. *Block Copolymers: Synthetic Strategies, Physical Properties and Applications*; Wiley: New York, 2003.
(3) Sioula, S.; Hadjichristidis, N.; Thomas, E. *Macromolecules* **1998**, *31* (23), 8429–8432.
(4) Sioula, S.; Hadjichristidis, N.; Thomas, E. *Macromolecules* **1998**, *31* (16), 5272–5277.
(5) Zioga, A.; Sioula, S.; Hadjichristidis, N. *Macromol. Symp.* **2000**, *157*, 239–249.
(6) Gemma, T.; Hatano, A.; Dotera, T. *Macromolecules* **2002**, *35*, 3225–3227.
(7) Yamauchi, K.; Takahashi, K.; Hasegawa, H.; Iatrou, H.; Hadjichristidis, N.; Kaneko, T.; Nishikawa, Y.; Jinnai, H.; Matsui, T.; Nishioka, H.; Shimizu, M.; Fukukawa, H. *Macromolecules* **2003**, *36* (19), 6962–6966.
(8) Takano, A.; Wada, S.; Sato, S.; Araki, T.; Hirahara, K.; Kazama, T.; Kawahara, S.; Isono, Y.; Ohno, A.; Tanaka, N.; Matsushita, Y. *Macromolecules* **2004**, *37* (26), 9941–9946.
(9) Yamauchi, K.; Akasaka, S.; Hasegawa, H.; Iatrou, H.; Hadjichristidis, N. *Macromolecules* **2005**, *38* (19), 8022–8027.
(10) Takano, A.; Kawashima, W.; Noro, A.; Isono, Y.; Tanaka, N.; Dotera, T.; Matsushita, Y. *J. Polym. Sci., Part B: Polym. Phys.* **2005**, *43* (18), 2427–2432.
(11) Hayashida, K.; Takano, A.; Arai, S.; Shinohara, Y.; Amemiya, Y.; Matsushita, Y. *Macromolecules* **2006**, *39* (26), 9402–9408.
(12) Hayashida, K.; Kawashima, W.; Takano, A.; Shinohara, Y.; Amemiya, Y.; Nozue, Y.; Matsushita, Y. *Macromolecules* **2006**, *39* (14), 4869–4872.
(13) Takano, A.; Kawashima, W.; Wada, S.; Hayashida, K.; Sato, S.; Kawahara, S.; Isono, Y.; Makihara, M.; Tanaka, N.; Kawaguchi, D.; Matsushita, Y. *J. Polym. Sci., Part B* **2007**, *45* (16), 2277–2283.
(14) Dotera, T.; Gemma, T. *Philos. Mag.* **2006**, *86*, 1085–109.
(15) Hayashida, K.; Dotera, T.; Takano, A.; Matsushita, Y. *Phys. Rev. Lett.* **2007**, *98* (19).
(16) Kirkensgaard, J. J. K.; Hyde, S. *Phys. Chem. Chem. Phys.* **2009**, *11*, 2016–2022.
(17) Hyde, S. T.; de Campo, L.; Oguey, C. *Soft Matter* **2009**, *5*.
(18) Hayashida, K.; Saito, N.; Arai, S.; Takano, A.; Tanaka, N.; Matsushita, Y. *Macromolecules* **2007**, *40* (10), 3695–3699.
(19) Espanol, P.; Warren, P. *Europhys. Lett.* **1995**, *30* (4), 191.
(20) Groot, R.; Madden, T. *J. Chem. Phys.* **1998**, *108* (20), 8713.
(21) Ortiz, V.; Nielsen, S.; Discher, D.; Klein, M.; Lipowsky, R.; Shillcock, J. *J. Phys. Chem. B* **2005**, *109*, 17708–17714.
(22) Abu-Sharkh, B.; AlSunaidi, A. *Macromol. Theory Simul.* **2006**, *15*, 507–515.
(23) Huang, C.; Yu, H. *Polymer* **2007**, *48*, 4537–4546.
(24) Huang, C.; Fang, H.; Lin, C. *Phys. Rev. E* **2008**, *77*, 031804.
(25) Klymko, T.; Markov, V.; Subbotin, A.; ten Brinke, G. *Soft Matter* **2009**, *5*, 98–103.
(26) Mortensen, K.; Theunissen, E.; Kleppinger, R.; Almdal, K.; Reynaers, H. *Macromolecules* **2002**, *35*, 7773–7781.
(27) Mortensen, K.; Vigild, M. E. *Macromolecules* **2009**, *42*, 1685–1690.
(28) Bellas, V.; Iatrou, H.; Hadjichristidis, N. *Macromolecules* **2000**, *33*, 6993.
(29) Bellas, V.; Iatrou, H.; Pitsinos, N. E.; Hadjichristidis, N. *Macromolecules* **2001**, *34*, 5376.
(30) Fragouli, P.; Iatrou, H.; Hadjichristidis, N.; Sakurai, T.; Matsunaga, Y.; Hirao, A. *J. Polym. Sci., Part A* **2006**, *44*, 6587–6599.
(31) Hadjichristidis, N.; Iatrou, H.; Pispas, S.; Pitsikalis, M. *J. Polym. Sci., Part A* **2000**, *38*, 3211.
(32) Groot, R.; Warren, P. *J. Chem. Phys.* **1997**, *107* (11), 4423.
(33) Huckstadt, H.; Göpfert, A.; Abetz, V. *Polymer* **2000**, *41* (26), 9089–9094.
(34) James, M. E. *Physical Properties of Polymers Handbook*, 2nd ed.; Springer: Berlin, 2007.
(35) Kirkensgaard, J. J. K. *Soft Matter* **2010**, DOI: 10.1039/c0sm00358a.
(36) Limbach, H. J.; Arnold, A.; Mann, B. A.; Holm, C. *Comput. Phys. Commun.* **2006**, *174* (9), 704–727.
(37) Hamley, I. *Phys. Rev. E* **1994**, *50* (4), 2872–2880.
(38) Koppi, K.; Tirrell, M.; Bates, F.; Almdal, K.; Mortensen, K. *J. Rheol.* **1994**, *38* (4), 999–1027.
(39) Hamley, I. W.; Koppi, K. A.; Rosedale, J. H.; Bates, F. S.; Almdal, K.; Mortensen, K. *Macromolecules* **1993**, *26*, 5959–5970.
(40) Zhu, L.; Huang, P.; Chen, W. Y.; Weng, X.; Cheng, S. Z. D.; Ge, Q.; Quirk, R. P.; Senador, T.; Shaw, M. T.; Thomas, E. L.; Lotz, B.; Hsiao, B. S.; Yeh, F.; Liu, L. *Macromolecules* **2003**, *36*, 3180–3188.
(41) Hamley, I. W.; Castelletto, V.; Mykhaylyk, O. O.; Gleeson, A. J. *J. Appl. Crystallogr.* **2004**, *37*, 341–344.
(42) Almdal, K.; Koppi, K.; Bates, F.; Mortensen, K. *Macromolecules* **1992**, *25*, 1743–1751.
(43) Hashimoto, T.; Koizumi, S.; Hasegawa, H.; Izumitani, T.; Hyde, S. *Macromolecules* **1992**, *25*, 1433–1439.
(44) Spontak, R. J.; Smith, S. D.; Ashraf, A. *Macromolecules* **1993**, *26*, 956–962.
(45) Disko, M.; Liang, K. S.; Behal, S. K.; Roe, R. J.; Jeon, K. J. *Macromolecules* **1993**, *26*, 2983–2986.
(46) Hamley, I. W.; Gehlsen, M. D.; Khandpur, A. K.; Koppi, K. A.; Rosedale, J. H.; Schulz, M. F.; Bates, F. S.; Almdal, K.; Mortensen, K. *J. Phys. II* **1994**, *4*, 2161–2186.
(47) Matsen, M. W.; Schick, M. *Phys. Rev. Lett.* **1994**, *72*, 2660–2663.
(48) Qi, S.; Wang, Z. G. *Phys. Rev. Lett.* **1996**, *76*, 1679–1782.
(49) Qi, S.; Wang, Z. G. *Phys. Rev. E* **1997**, *55*, 1682–1697.
(50) Matsen, M. W.; Bates, F. S. *J. Chem. Phys.* **1997**, *106*, 2436–2448.
(51) Vigild, M. E.; Almdal, K.; Mortensen, K.; Hamley, I. W.; Fairclough, J. P. A.; Ryan, A. J. *Macromolecules* **1998**, *31*, 5702–5716.
(52) Hajduk, D. A.; Ho, R. H.; Hillmyer, M. A.; Bates, F. S.; Almdal, K. *J. Phys. Chem. B* **1998**, *102*, 1356–1363.
(53) Wang, C. Y.; Lodge, T. P. *Macromolecules* **2002**, *35*, 6997–7006.
(54) Eskimergen, R.; Mortensen, K.; Vigild, M. E. *Macromolecules* **2005**, *38*, 1286–1291.
(55) Mareau, V. H.; Akasaka, S.; Osaka, T.; Hasegawa, H. *Macromolecules* **2007**, *40*, 9032–9039.